scientific reports

Compact flexible linear stepping motors

Cheng-Lung Chen[1], Shen-Yun Chu[2], Yao-Te Tsai[1] & Shao-Kang Hung[1]✉

Flexible actuators capable of bending, twisting, and stretching have garnered significant interest for applications in wearable and mobile devices. In this study, we present the development of flexible linear stepping motors (FLSMs) with moving sliders fabricated from flexible printed circuit boards as thin as 0.1 mm. The force output of these motors can be enhanced by stacking multiple sliders, and their operational stroke length is theoretically unlimited. Experimental results demonstrate a maximum speed of 500 mm/s, a step size of 25 µm, and a force constant of 743 mN/A. Notably, the proposed device achieves the highest volumetric force constant of 5.94 mN/A(mm)^3 reported in the literature. The flexibility and compact design of these FLSMs make them particularly suitable for space-constrained applications, such as actuators in robotic fingers and pupillary distance adjusters in virtual reality headsets.

Stepping motors are widely employed across various fields due to their cost-effectiveness and open-loop positioning capabilities. They function effectively without sensor feedback, provided that synchronization losses are consistently avoided. The introduction of the well-known micro-stepping technique[1–4] has significantly improved the resolution of stepping motors without compromising speed. Consequently, a diverse range of stepping motors with varying specifications has been developed, establishing them as standard components in numerous applications, including 3D printing[5], nano-manipulation[6], robotics[7], and magnetic resonance imaging[8]. These applications have also utilized state-of-the-art actuators, including dielectric elastomer actuators (DEA)[9,10], shape memory alloys (SMA)[11,12], and piezoelectric miniature rotary motors[6]. However, DEA requires a relatively high operating voltage. SMA, which relies on temperature changes for deformation, exhibits slow response speed under conditions of poor heat dissipation. Additionally, miniature rotary motors necessitate extra mechanisms to convert rotational motion into linear displacement. Given these limitations, this article focuses on low-voltage-driven stepping motors, which enable fast and direct linear motion.

Unlike traditional enameled wires wound around solid yokes, FPCB offers the potential to create slim and flexible windings. As depicted in Fig. 1, an FPCB is a laminated sandwich structure composed of conductive and insulating layers, with the conductive patterns processed through photolithography, similar to rigid printed circuit boards (PCBs). Polyimide (PI), known for its excellent thermal stability, is the most commonly used material for the insulating layers in FPCBs, enabling operation at high temperatures. The number of layers determines the total thickness, which is typically kept below several hundred microns to maintain flexibility. With a mature fabrication process, FPCBs are now extensively utilized in wearable devices, consumer electronics, and soft robots[13,14].

Both rigid PCBs and FPCBs can be fabricated into planar coils, which are then used as inductive[15–17], resistive[18–20], and bioelectric[21–23] sensors. Due to their inherent flexibility, FPCBs also serve as actuators, particularly in applications such as laser scanners[28] and LiDAR[29]. Common planar coil shapes include circular and rectangular configurations, while trapezoidal and rhomboidal coils[30,31] have been developed to enhance performance. Additionally, three-segment and sinusoidal winding patterns[32] have been proposed to reduce force ripple in tubular permanent magnet (PM) synchronous motors. The literature indicates that FPCBs are capable of realizing various types of actuators; however, these designs often incorporate "vias," which introduce certain drawbacks.

As illustrated in Fig. 1, a “via” is a vertical hollow cylindrical wall with chemically deposited copper that connects horizontal conductive layers. This thin copper coating has relatively higher resistance, which can become a bottleneck for electric conductivity, particularly after repeated deformation[33]. When the motor operates at high currents, vias generate excessive heat, thereby degrading overall performance[34]. To address these issues, we propose a novel via-free S-shape (VFSS) winding pattern and utilize it to develop ultra-slim linear stepping motors based on FPCBs. Our survey identified the earliest use of the VFSS winding pattern in Hitachi’s uni-torque motor[35], where it was employed as a single-phase speed detection unit. In this work, we

[1]Department of Mechanical Engineering, National Yang Ming Chiao Tung University, 300, Hsinchu City, Taiwan. [2]Global Support Center, ASML Holding N. V., Veldhoven 5504, The Netherlands. ✉email: skhung@nycu.edu.tw

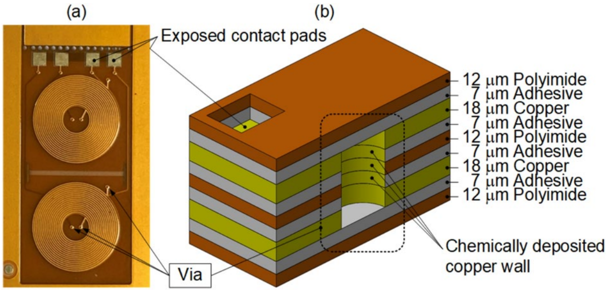

Fig. 1. (**a**) The photograph of a typical FPCB containing circular coils with several vias. (**b**) The cross-section of the FPCB showing the inner structure of a vertical "via" which conducts electricity between copper layers.

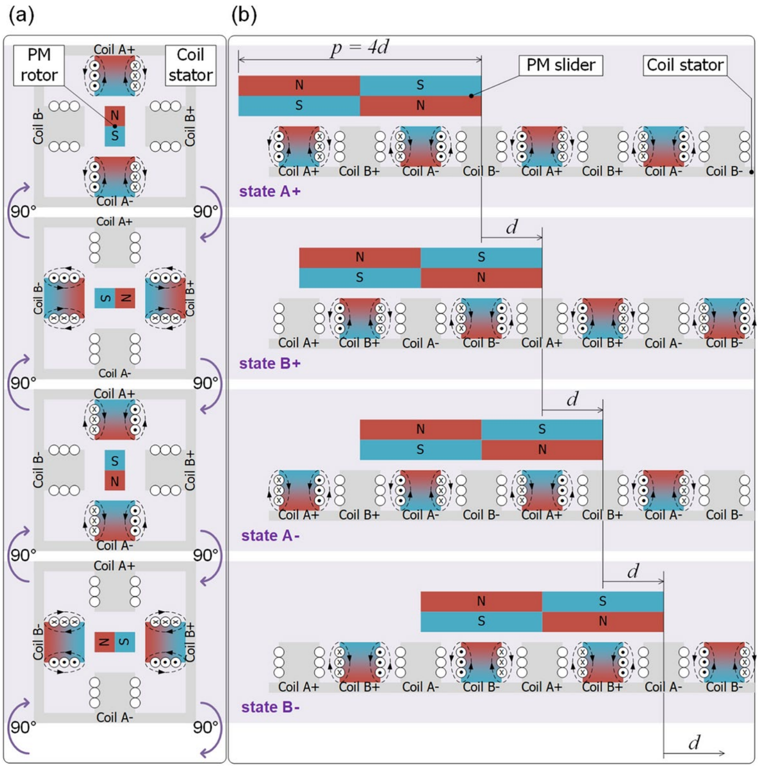

Fig. 2. (**a**) Working principle of a rotary stepping motor. (**b**) Working principle of a linear stepping motor.

innovatively transform the multi-phase VFSS winding pattern from a sensing unit into an actuating unit for the first time.

Results

VFSS winding pattern

Figure 2a illustrates the working principle of a typical 2-phase bipolar rotary stepping motor. The coils function as the external stator, while the PM forms the central rotor shaft. Coil A+ and Coil A− are connected in series, as are Coil B+ and Coil B−. First, when Coil A+ and Coil A− are positively energized, Coil A+ attracts the N pole of the PM rotor, while Coil A− attracts the S pole. Second, when Coil B+ and Coil B− are positively energized, Coil B+ attracts the N pole, and Coil B− attracts the S pole. At this point, the rotor advances by one step (90°) from its initial position. Third, when Coil A+ and Coil A− are negatively energized, Coil A+ attracts the S pole, while Coil A− attracts the N pole, causing the rotor to turn another 90° clockwise (CW). Fourth, when Coil B+ and Coil B− are negatively energized, Coil B+ attracts the S pole, while Coil B− attracts the N pole, leading to another 90° CW rotation. Returning to the initial state completes one full cycle. The sequential activation of the coils results in incremental rotor movement. By reversing the activation sequence, the rotor rotates in the counterclockwise (CCW) direction. The details of stepping motors and their driving circuits are comprehensively covered in[36].

The aforementioned 4-state working principle can be extended from rotational to translational motion, as illustrated in Fig. 2b. In this configuration, the coils function as the stator placed beneath the PM slider.

Transitioning to the next activation state causes the coils to attract the corresponding PM poles, resulting in the PM slider stepping rightward by a distance *d*. For a typical 2-phase structure, the relationship between the pitch *p* of the periodic coil array and the step distance is given by $p = 4d$, where *p* also corresponds to twice the width of a PM element. Consequently, completing one full pitch requires four steps. By reversing the 4-state activation sequence, the sliding direction changes to leftward motion.

Leveraging the aforementioned benefits of FPCB, we extend the working principle of traditional stepping motors (Fig. 2) to FPCB-based stepping motors (Fig. 3). The most intuitive approach is to replicate the "coil-shaped" winding pattern in a planar FPCB design. As magnified in Fig. 3(a), the A+ coil-shaped winding spirals inward CW on the top layer, connects to the bottom layer through a via, and then spirals outward CW. The winding shape can be circular, rectangular, or other polygonal forms. To generate the alternating magnetic field required in Fig. 2b, the winding directions of Coil B+, Coil A−, and Coil B− are also illustrated in Fig. 3a. However, this intuitive approach has two major drawbacks: (1) the presence of vias, which may introduce fabrication complexity and electrical resistance, and (2) a long pitch, resulting in a large step size, whereas smaller steps are preferable for precise position control.

To address these issues, we propose a VFSS winding pattern in Fig 3b. Similar to the letter "S," the copper trace first bends 180° CCW and then 180° CW, generating an alternating magnetic field. A series of S-shaped traces on the top layer forms phase A, while another set of quad-pitch-shifted S-shaped traces on the bottom layer forms phase B. The operating principle of this structure follows the same activation sequence as depicted in Fig. 3c, analogous to Fig. 2b. Compared to the coil-shaped winding in Fig. 3a, the S-shaped copper trace reduces the pitch length, resulting in a smaller step size. Furthermore, by eliminating the need for interlayer connections, this via-free design effectively avoids the drawbacks associated with vias, such as increased electrical resistance and fabrication complexity.

Furthermore, the number of phases is directly proportional to the number of steps required to complete a cycle[28]. This implies that for a given pitch length, increasing the number of phases divides the movement into more steps, thereby reducing the step size. However, an excessive number of phases can lead to higher costs, a reduced yield rate, and a loss of flexibility. To strike a balance, we selected a 5-phase configuration for the second version. The working principle is illustrated in Fig. 4 with five windings in the FPCB stator. Transitioning to the next activation state causes the coils to attract the corresponding PM poles, advancing the PM slider rightward by a distance *d*. In this 5-phase structure, the relationship between the pitch *p* and the step distance is given by $p = 10d$. As a result, completing one full cycle requires 10 activation states, leading to a step size one-tenth of the pitch. Compared to the 2-phase version, the 5-phase version offers smaller step size, higher acceleration, lower

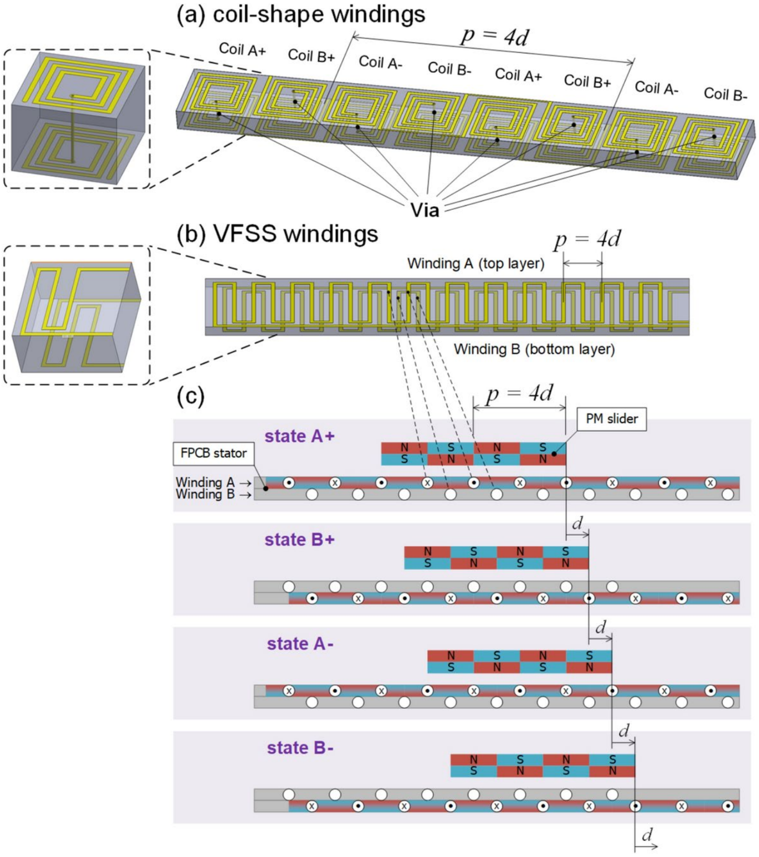

Fig. 3. (**a**) Traditional planar coil-shape windings with vias. (**b**) Novel via-free S-shape (VFSS) winding pattern. (**c**) Working principle of a 2-phase linear stepping motor made with VFSS FPCB windings.

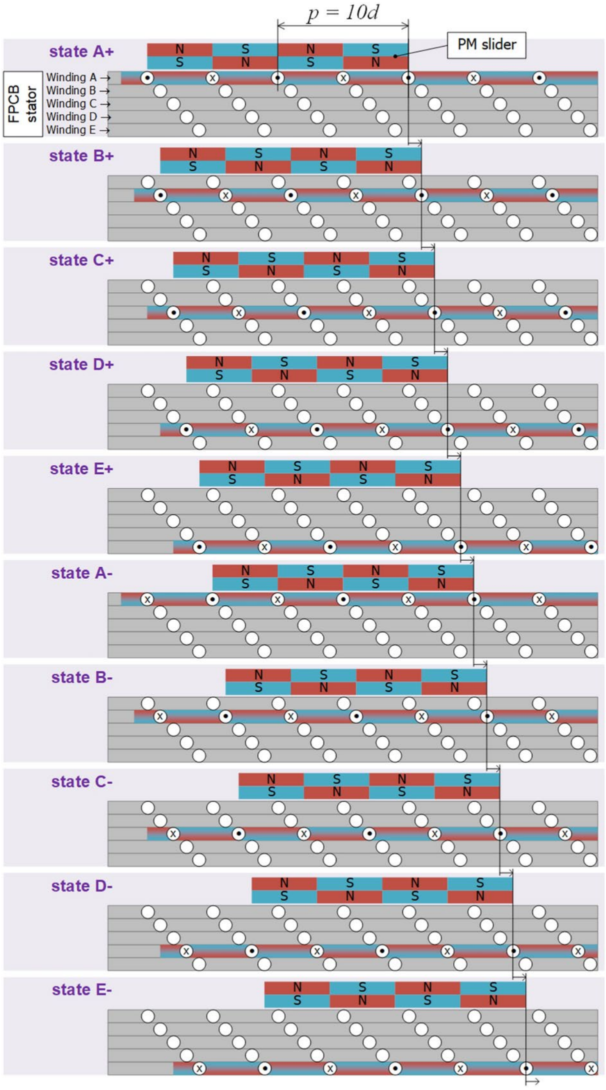

Fig. 4. Working principle of a 5-phase linear stepping motor made with VFSS FPCB windings. There are 10 fine steps to move a pitch.

overshoot, and a reduced likelihood of synchronization loss[37]. Additionally, the driving circuitry of a pentagon connection[37,38], commonly used in 5-phase stepping motors, is readily available in the market.

Conceptual prototype

Compared with the PM array, the lightweight FPCB is more suitable to be the moving part; therefore, we reverse the roles of the slider and stator in our prototype design. Figure 5 and the Supplementary Video S1 illustrate its operation. One end of the FPCB strip is fixed to a gantry and connected to an electrical driver, while the other end performs a reciprocating motion along the PM array. The speed and moving range are controlled by the driver's program. Notably, the FPCB slider maintains direct contact with the PM array due to the attractive force between them. A lithium-based lubricant is applied to reduce friction. Throughout the remainder of this article, the FPCB functions as the slider, flexing and stretching across the surface of the PM array stator. The FPCB can also slide along a "curved" PM rail, with a concave left section and a convex right section. Furthermore, two FPCB sliders are driven synchronously or independently, moving together as a combined unit or allowing for separate movements.

Formal design

The initial conceptual prototype demonstrates feasibility, but its single-sided PM structure results in magnetic field lines leaking into open space. To enhance the magnetic flux intensity, a double-sided PM structure is employed in the final designs. The measured surface magnetic flux density for the single-sided and double-sided versions is 210 mT and 620 mT, respectively. This nearly threefold increase confirms the effectiveness of the double-sided PM structure in enhancing magnetic flux density. As shown in Fig. 6, the thin FPCB slider is positioned within a strong magnetic field between two PM arrays. 3D-printed spacers withstand the attractive

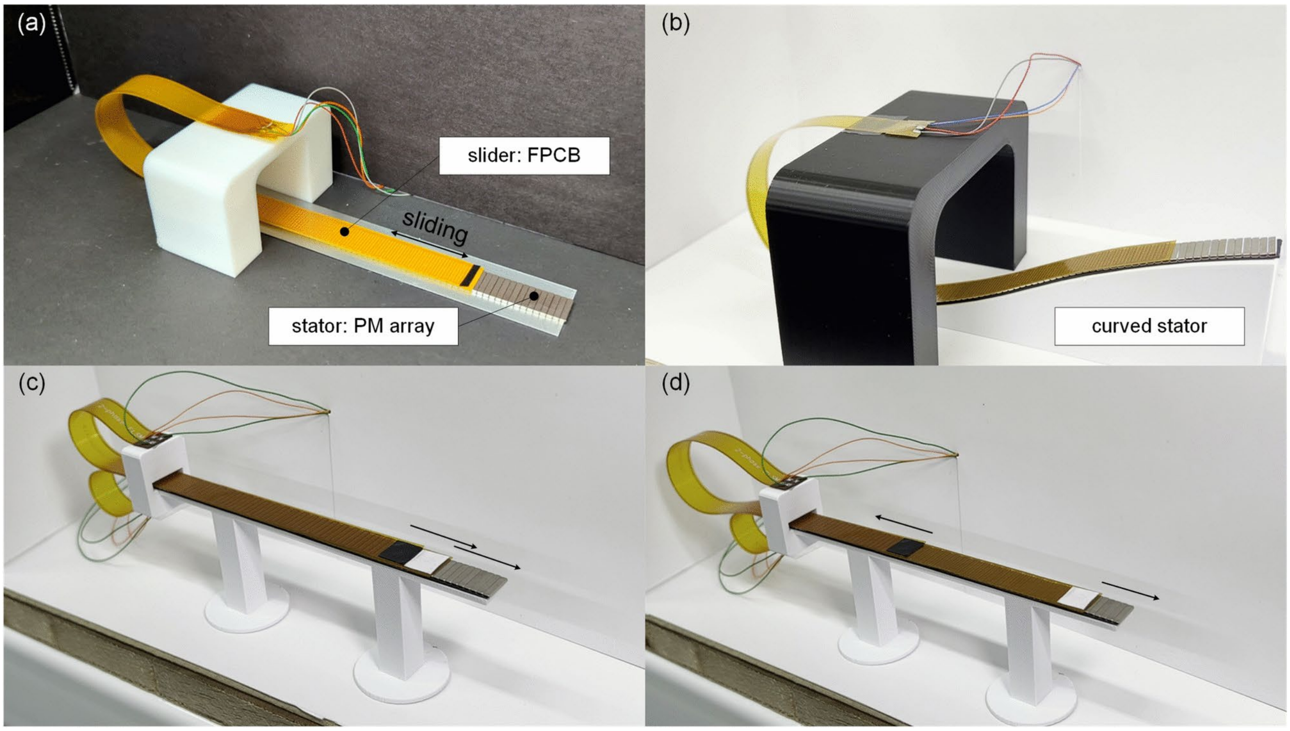

Fig. 5. The conceptual prototype: (**a**) The FPCB slides on a flat PM array. (**b**) The FPCB slides on a curved PM array. (**c**) Two FPCB sliders work toward the same direction. (**d**) Two FPCB sliders work toward opposite directions. In the PDF version of this article, please click anywhere on the figure or caption to play the video in a separate window.

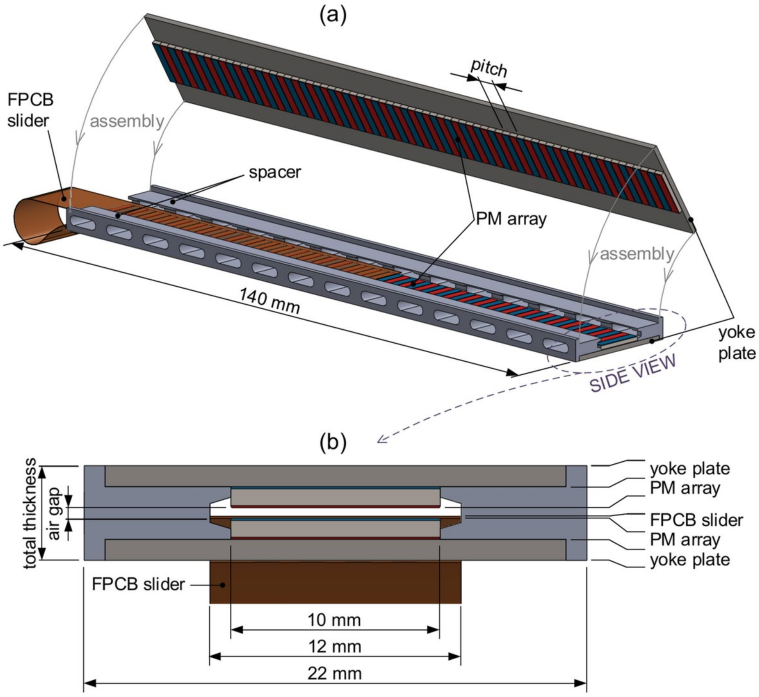

Fig. 6. (**a**) The inner structure and (**b**) the side view of the proposed linear stepping motor.

	2-Phase version	5-Phase version
Winding layers	2	5
PM material	Nd–Fe–B	Nd–Fe–B
FPCB insulation material	PI	PI
Yoke material	Cold rolled steel	Cold rolled steel
Active region	80 mm × 10 mm	50 mm × 10 mm
Full-step size / PM pitch	1 mm/4 mm	0.2 mm/2 mm
Phase shift/winding pitch	1 mm/4 mm	0.2 mm/2 mm
Trace width (μm)	250	200
Trace thickness (μm)	18	18
FPCB thickness (μm)	100	250
PM thickness (mm)	1	2
Yoke plate thickness (mm)	1	1
Air gap (mm)	0.5	0.5
System total thickness (mm)	4.5	6.5

Table 1. Design parameters of the proposed devices in this work.

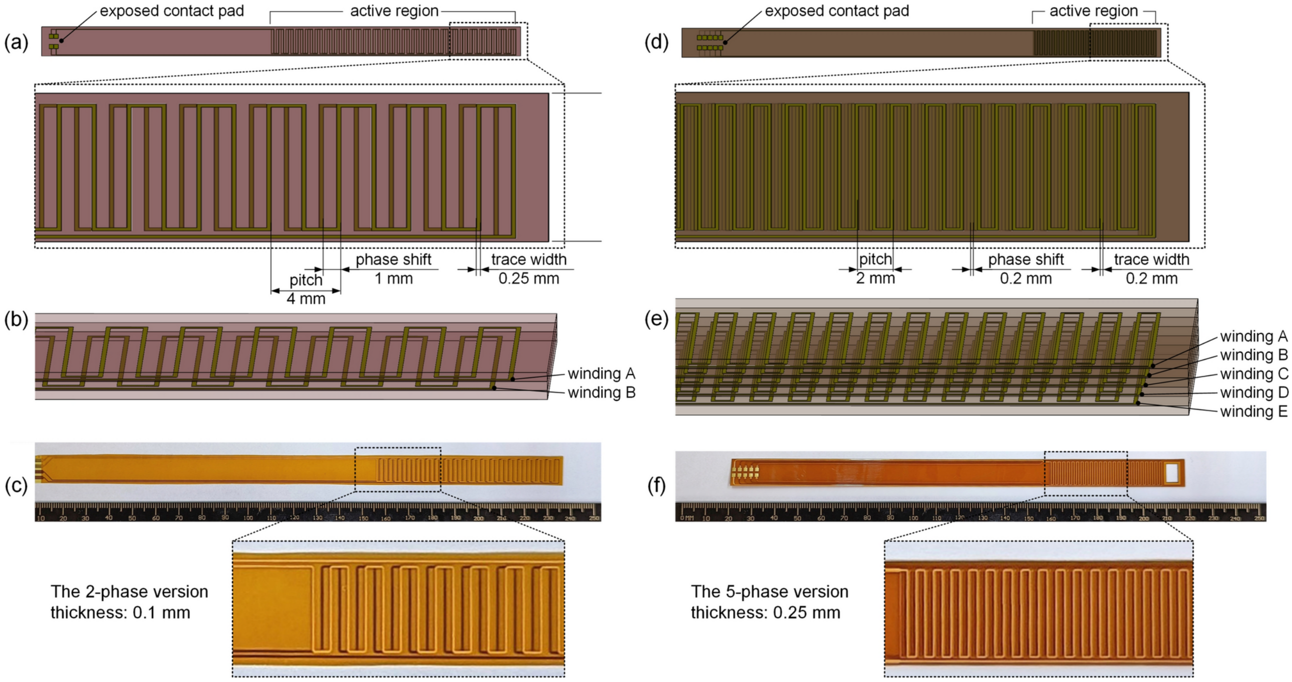

Fig. 7. (**a**) The top-view, (**b**) the tiled side view, and (**c**) the photograph with enlargement of the 2-phase FPCB slider. (**d**) The top-view, (**e**) the tiled side view, and (**f**) the photograph with enlargement of the 5-phase FPCB slider. To show the inner structures clearly, thickness in (**b**) and (**e**) is not to scale.

force between the PM arrays and create a narrow air gap, allowing the FPCB to slide through. The outer yoke plates, fabricated from cold-rolled steel, minimize magnetic leakage and dissipate heat. The detailed design parameters for the proposed 2-phase and 5-phase versions are listed in Table 1 and illustrated in Fig. 7.

Positioning character

Precision is the foremost performance metric for stepping motors, as users demand a consistent and small step size per trigger. The proposed devices of 2-phase and 5-phase versions were tested under three modes supported by common stepping motor drivers: full-step, half-step, and 1/8-step modes[1,4]. Each test was repeated 100 times using an automated program. In Figs. 8 and 9, the central dots represent the mean values, while the standard deviation bars indicate the statistical variability of the results.

Figure 8 illustrates the positioning characteristics of the 2-phase flexible stepping motor. In the basic full-step mode, four full steps are needed to move a distance equivalent to one pitch, 4000 μm, with a displacement per step closely matching the theoretical value of 1000 μm. In the half-step mode, twice the number of half-steps is required to cover the same distance, but the step size exhibits greater variability. The motion in the 1/8-step

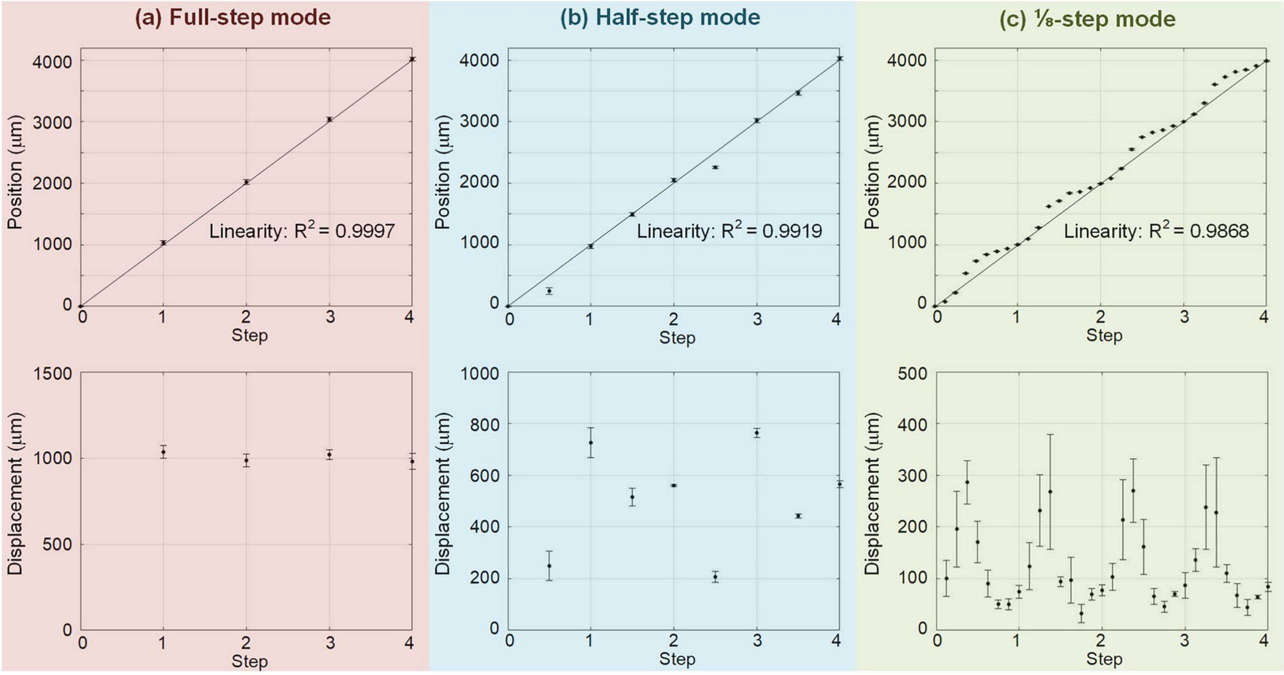

Fig. 8. The position and the displacement of the proposed 2-phase FLSM in (**a**) the full-step mode, (**b**) the half-step mode, and (**c**) the 1/8-step mode.

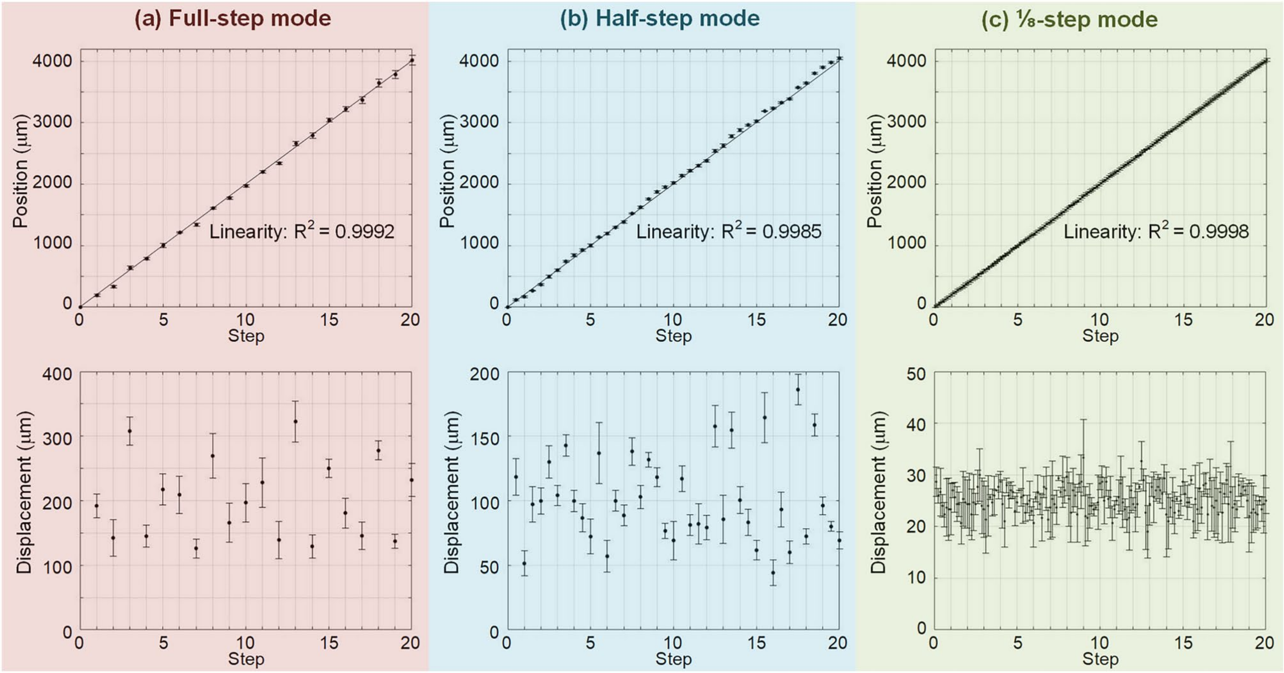

Fig. 9. The position and the displacement of the proposed 5-phase FLSM in (**a**) the full-step mode, (**b**) the half-step mode, and (**c**) the 1/8-step mode.

mode, which shows less linearity, is represented by the green-shaded column. Fig. 9 illustrates the corresponding performance of the 5-phase version. In the basic full-step mode, 20 full steps are required to move a distance equivalent to one pitch, 4000 μm. In the half-step mode, 40 half-steps are needed to cover the same distance. In the 1/8-step mode, 160 1/8-steps are required to traverse 4000 μm, exhibiting high linearity. The linearity defined by the coefficient of determination[39], denoted R^2, is the square of the correlation coefficient between the measured data and the theoretically linear model. In the context of stepping motors, perfect 100% linearity indicates identical step sizes, ensuring that the position is entirely determined by the number of steps.

When manually rotating the shaft of a common 2-phase rotary stepping motor, one may experience a stuttering or irregular sensation due to the presence of alternating stable and unstable regions, which is an inherent characteristic of stepping motors. This phenomenon, known as detent torque, arises from the generation of reluctance torque. As observed in Fig. 8c for the 2-phase 1/8-step mode, the position chart exhibits alternating low-slope and high-slope regions. The low-slope regions correspond to stable zones, where the position remains relatively resistant to external disturbances. In contrast, the high-slope regions indicate unstable zones, where small perturbations can cause noticeable positional shifts. This detent effect negatively impacts the motion linearity of the 2-phase FLSM. In contrast, the 5-phase version benefits from the previously described inter-phase compensation effect, which effectively enhances motion linearity, reducing the impact of the detent phenomenon.

Force-speed relation

Force and speed are also critical performance indicators for linear stepping motors, and they are typically negatively correlated, meaning that the motor can achieve higher speeds when operating under lighter loads. Figure 10 presents the force-speed curves of the 2-phase and 5-phase versions. In the experiment, the motor speed was controlled by an electrical motor driver, commanded by a computer program. The force was determined by the applied load, specifically the amount of standard weight placed in the weighing pan, as detailed in the Experimental Environment Section. Each data point represents the maximum force the FLSM can generate at a given speed. For the 2-phase version, the no-load maximum speeds are 250 mm/s, 400 mm/s, and 500 mm/s under the aforementioned three modes, respectively. The static holding force is at 168 mN across all modes. The maximum output power, calculated as the product of force and speed, reaches 8 mW. The input electrical power is estimated at 736 mW, resulting in an energy conversion efficiency of 1.1%. For the 5-phase version, where the 1/8-step mode achieves both stronger force and higher speed compared to the other two modes, with a maximum speed of 500 mm/s. The peak holding force is 297 mN, which is 37.9 times the weight of the FPCB itself. The highest output power is 17 mW, occurring at the midpoint of the force-speed curve. The input electrical power remains 736 mW, yielding an energy conversion efficiency of 2.3%.

The force-speed characteristics presented in Fig. 10 were measured under a phase current of 0.4 A. A comparison of force-speed characteristics at different current levels is provided in Supplementary Fig. S2. For both the two-phase and five-phase versions, the output force is approximately proportional to the phase current, confirming a linear relationship between these parameters.

As with all types of stepping motors, the force-speed relationship in the proposed devices is negatively correlated, with the area beneath the force-speed curve representing the workable zone. For the 2-phase version, there is no significant difference in performance among the full-step, half-step, and 1/8-step modes. However, for the 5-phase version, the 1/8-step mode exhibits the highest actuating force due to the following reasons: (1) The 5-phase version has more layers and denser windings than the 2-phase version, enabling greater mechanical output. (2) Unlike the full-step mode, which employs square waveforms, the 1/8-step mode utilizes quasi-sinusoidal waveforms across all five windings simultaneously. The smoother waveform reduces overshoot between steps, and the force ripple in each phase is compensated by other phases.

We refer to this phenomenon as the "inter-phase compensation effect," which ensures that no significant weak force moment occurs, thereby preventing synchronization loss and significantly increasing the output force. The presence of more phases enhances the inter-phase compensation effect, which also contributes to improved motion accuracy and repeatability by balancing the positioning errors across phases. This is the underlying reason why the 5-phase version in 1/8-step mode demonstrates the best performance.

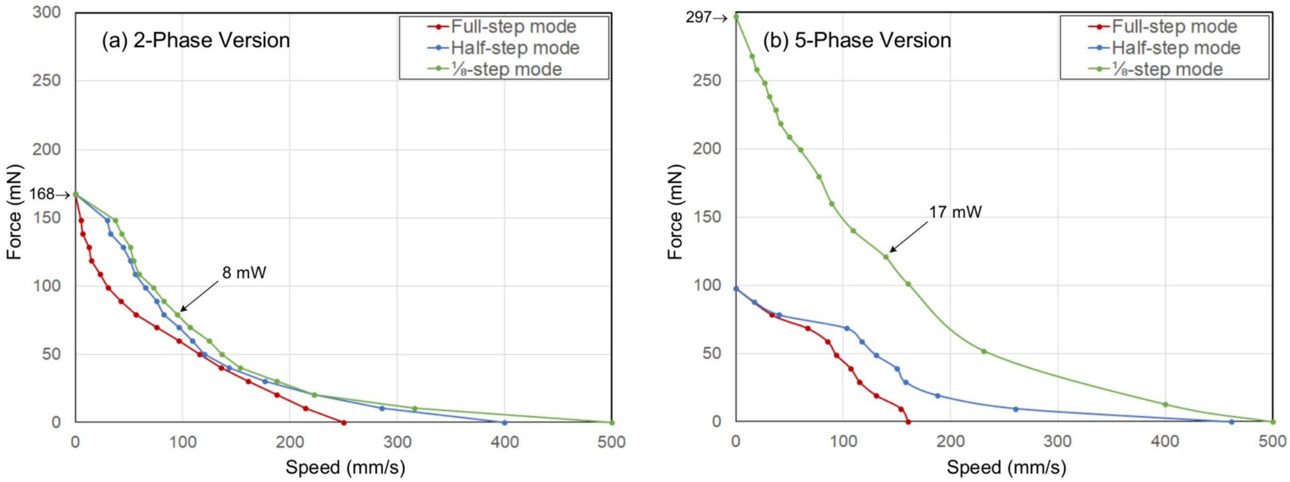

Fig. 10. The force-speed curves of the proposed (**a**) 2-phase and (**b**) 5-phase FLSM.

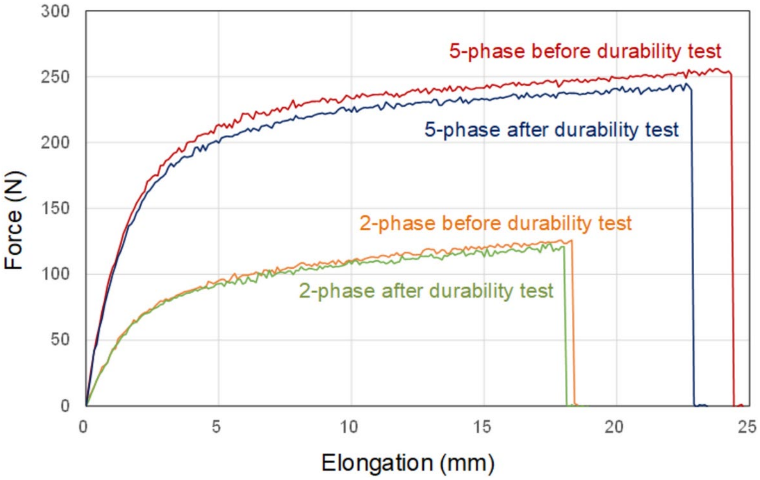

Fig. 11. The tensile testing curves of the 2-phase and 5-phase FPCB sliders. Their strength is greater than 100 N after 10 million times operation.

	Full-step mode	Half-step mode	1/8-step mode
2-Phase version			
Motion linearity (%)	99.97	99.19	98.68
Step size (average) (μm)	1004.8	503.6	125.1
Step size (σ) (μm)	44.1	190.3	87.7
Max force (mN)	168	168	168
Max speed (mm/s)	250	400	500
5-Phase version			
Motion linearity (%)	99.92	99.85	99.98
Step size (average) (μm)	200.7	101.2	25.0
Step size (σ) (μm)	64.6	33.7	4.7
Max force	98 N	98 N	297 mN
Max speed (mm/s)	160	461	500

Table 2. Experimental results of the proposed devices.

Durability

The repeated stretching and flexing motion of FPCB raise concerns about potential fatigue[40]. To demonstrate durability, we tested the proposed devices by subjecting them to reciprocating motion at 1 Hz for 120 days. Due to the significant time required for testing, only a single specimen of each version was evaluated. To achieve the highest possible speed, tests were conducted without any applied load, and the 1/8-step mode was selected. After completing 10 million cycles of full-stroke, 100 mm, both the 2-phase and 5-phase versions remained fully functional without any mechanical or electrical failures. Subsequently, the FPCB strips were disassembled from the system and tested using a tensile testing machine (MTS 810, MTS Systems Corporation), with the results shown in Fig. 11.

Before the durability test, the breaking points were recorded as 125 N for the 2-phase FPCB strip and 255 N for the 5-phase FPCB strip. After the durability test, the breaking points slightly decreased to 120 N and 240 N, respectively. These results indicate that after 10 million cycles, the strength of the proposed devices degrades 4% ~ 6% and still significantly exceeds the forces they can generate. Therefore, we conclude that our FLSM exhibit excellent durability.

Summary of results

Table 2 summarizes the experimental results of this study. Among all configurations, the 5-phase version operating in the 1/8-step mode demonstrates the most outstanding performance. It achieves near-perfect motion linearity at 99.98%, while the fine step size of 25 μm provides excellent precision. The ultralow standard deviation of 4.7 μm indicates robust repeatability. The speed of 500 mm/s, corresponding to a stepping frequency of 20 kHz or 50 μs/step, suggests the capability for dynamic adjustment of optical elements. Additionally, the output force of 297 mN defines the maximum payload the device can lift. In summary, the 5-phase version in 1/8-step mode is the superior choice for high-end applications, provided this mode is available. Conversely, the

2-phase version offers simplicity and lower fabrication costs. Both versions demonstrate a lifespan exceeding 10 million operations.

Among the surveyed literature on FPCB linear motors, only Hsu et al.[31] successfully reported experimental results. Table 3 compares the major specifications of Hsu's work with our own. While Hsu did not measure speed or force directly, they recorded the peak value of the back electromotive force in V/m·s^{-1}, assumed an ideal 100% electrical-to-mechanical energy conversion, and derived an indirect force constant of 633 mN/A. In practice, the actual value is likely lower due to factors such as iron loss, copper loss, and friction on the guiding rails. Our measured force constant for the 5-phase version is 743 mN/A, representing a 17.4% improvement. Furthermore, when considering the active area, our areal force constant of 1.49 mN/A(mm)^2 demonstrates superior performance, indicating that the proposed phase-shifted VFSS winding pattern effectively achieves high areal density.

Additionally, a high volumetric force constant is desirable, as it implies that a smaller actuator can generate significant force. Table 3 shows that our via-free design exhibits much higher volumetric force constants in both versions. This advantage can be attributed to the following: in standard FPCB manufacturing processes, chemically deposited copper atoms create bumps around both ends of a via, significantly increasing the thickness and reducing the available space for additional active copper winding layers. This inefficiency results in a high thickness-per-phase value of 0.167 mm. In contrast, our via-free design achieves a much thinner thickness-per-phase value of 0.05 mm, saving space and contributing to an outstanding volumetric force constant of 5.94 mN/A(mm)^3—a 209% improvement compared to the 1.92 mN/A(mm)^3 of a conventional non-via-free design.

Discussion

In this research, a phase-shifted VFSS winding pattern was designed, analyzed, and implemented in the moving FPCB sliders of the proposed FLSMs. This design offers several advantages, including space-saving, low inertia, high speed, fine precision, and excellent specific force output. The experiments demonstrated that the maximum speed, linearity, step size, repeatability, force constant, and lifespan achieved were 500 mm/s, 99.98%, 25 µm, 4.7 µm, 743 mN/A, and 10 million cycles, respectively. Under the 1/8-step mode, the proposed 5-phase version exhibits the highest areal and volumetric force constants among the surveyed literature.

Compared to traditional coil-shaped windings, the proposed VFSS design effectively eliminates via-related drawbacks, such as electrical conductivity bottleneck and inefficient space utilization. As a result, the VFSS-based FLSM achieves a higher force-to-volume ratio. Compared to the 2-phase version, the primary factor contributing to the superior performance of the 5-phase version is the stronger inter-phase compensation effect. Increasing the number of phases enhances overall performance, providing smoother motion and improved linearity. With the current state of technology, most FPCB manufacturers support mass production of 2- to 5-layer designs, making the proposed approach feasible for practical implementation.

This article presents novel linear stepping motors featuring FPCB and experimentally investigates the performance of a single slider. In future work, we will explore FLSMs with multiple ultrathin FPCB sliders,

	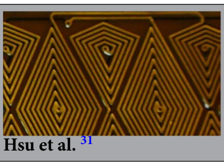 **Hsu et al.** [31]	 **2-Phase version of this work**	 **5-Phase version of this work**
Design parameters			
FPCB via design	With vias	via-free	via-free
Stroke (mm)	60	100	100
Winding phases (P)	3	2	5
Phase resistance (R) (Ω)	4.6	4.6	4.6
FPCB active length (L) (mm)	30	80	50
FPCB active width (W) (mm)	22	10	10
FPCB thickness (T) (mm)	0.5	0.1	0.25
Thickness per phase (T/P) (mm)	0.167	0.05	0.05
Phase current (I)	Not provided	0.4 A	0.4 A
Power			
Output mechanical power (P)	Not provided	8 mW	17 mW
Input electrical power (I^2R)	Not provided	736 mW	736 mW
Energy conversion efficiency (P/I^2R)	Not provided	1.1%	2.3%
Force			
Output force (F)	Not measured	168 mN	297 mN
Force constant (F/I)	633 mN/A	420 mN/A	743 mN/A
Areal force constant (F/ILW)	0.96 mN/A(mm)^2	0.525 mN/A(mm)^2	1.49 mN/A(mm)^2
Volumetric force constant (F/ILWT)	1.92 mN/A(mm)^3	5.25 mN/A(mm)^3	5.94 mN/A(mm)^3

Table 3. Force output comparison among FPCB linear motors.

which lead to electrical and mechanical benefits. With multiple windings per phase, the classical pole-changing technique can be applied to switch between high-force mode and high-speed mode for variable operations. When these sliders are driven synchronously, their combined force can be summed to carry heavier loads. Alternatively, independent control of the sliders could enable complex motions with multiple degrees of freedom. Potential applications include antagonistic artificial muscles, oscillating fins for robotic fish, crawling legs for robotic insects, and ultrathin XY-tables.

Regarding the potential challenges and limitations, one of the primary considerations is the thermal effect. The output force per slide is proportional to the driving current, whereas the heat generation is proportional to the square of the current. This relationship implies that a significant increase in temperature could lead to PM demagnetization and mechanical degradation of PI films. To mitigate these risks, an appropriate current limitation must be established based on the thermal analysis discussed in the next section.

Methods

Fabrication of the FPCB

For the 2-phase version, the FPCB slider consists of an inner 12 μm thick PI layer, sandwiched between copper foils on both sides. The copper foils have a thickness of 18 μm, equivalent to 0.5 oz/ft^2. The total thickness of the 2-phase FPCB slider is 100 μm, with the remaining thickness contributed by epoxy adhesives which bond different layers together, as outlined in Fig. 1. The trace width, phase shift, and winding pitch are 0.25 mm, 1 mm, and 4 mm, respectively. For the 5-phase version, the PI layers and copper foils remain at 12 μm and 18 μm, respectively, similar to the 2-phase version. However, the total thickness of the 5-phase FPCB slider is 250 μm. In this version, the trace width, phase shift, and winding pitch are 0.2 mm, 0.2 mm, and 2 mm, respectively. The FPCB samples used in this work were manufactured by Sunflex Tech Co., Ltd.

Inspection of the FPCB

The step size is determined by the pitch of the periodic coil array. Users expect a uniform step size; however, imperfections in FPCB fabrication introduce variability in the experimental step size, accompanied by a standard deviation. The FPCB samples were inspected using an optical microscope (BX51, Olympus) equipped with an industrial camera (DFK22AUC03, Imaging Source). Figure 12 shows a qualified sample with uniformly interlaced windings alongside a defective sample with noticeable misalignment between adjacent windings. The dependency of positioning accuracy on manufacturing quality is a well-known issue in all types of stepping motors. Although screening the quality of FPCB samples can enhance the consistency of the step size, it presents a trade-off between performance and cost.

Experimental environment

As shown in Fig. 13, the proposed linear stepping motor is mounted on a chilled aluminum base, maintained at a temperature below 50 °C using a liquid circulation cooling chiller. The FPCB slider carries the end-point reflector, whose motion is measured by a precision laser displacement sensor (LK-H020 + LK-HD500, Keyence) with 20 nm accuracy and a 6 mm range. A pulley-mounted weighing pan applies a rightward pulling force on the FPCB slider via a string. The loading force is gradually increased by adding standard weights to the pan, with a minimum increment of 1 gram. Each phase winding is driven by an H-bridge coil driver (L298N, STMicroelectronics), controlled by a microcontroller (ESP32, Espressif) with 32 kHz pulse width modulation (PWM). In practice, the winding resistance of each phase exhibits slight variations. To maintain a constant current of 0.4 A per phase, a 0.1 Ω shunt resistor is connected to each winding to measure its current, which is then fed back to the microcontroller. The microcontroller adjusts the PWM duty cycle based on the feedback from each shunt resistor to ensure consistent phase currents. The achievement of constant phase current has been verified using a current meter (DAQ6510, Keithley).

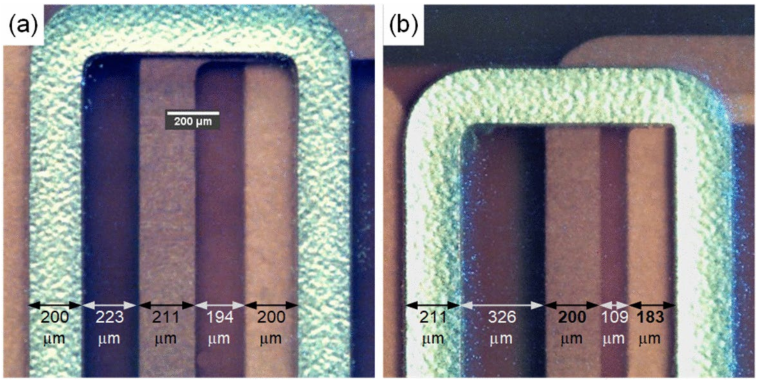

Fig. 12. The optical inspection images of the 5-phase FPCB sliders. (**a**) A qualified sample: five layers of windings interlace uniformly with little misalignment. (**b**) A unqualified sample: obvious misalignment between layers.

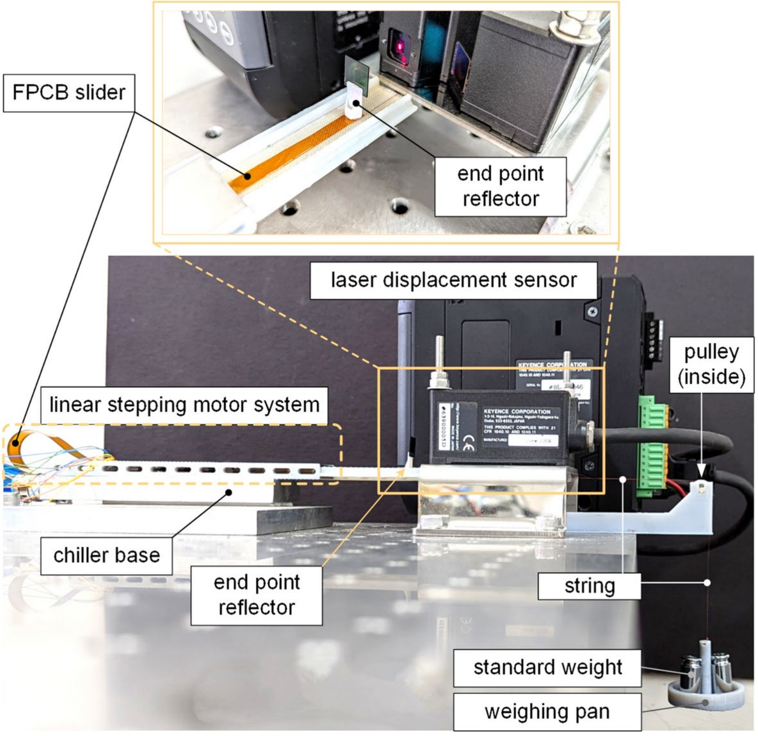

Fig. 13. The photograph of the experimental setup in this work. The pulleyed standard weights provide the adjustable loading force. The flexible linear stepping motor carries an end point reflector whose motion is measured by a laser displacement sensor.

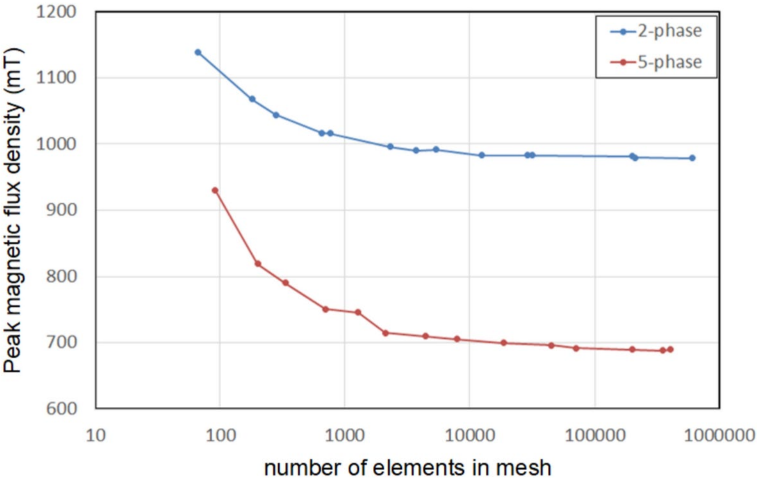

Fig. 14. The mesh convergence diagram of the finite element analysis.

Finite element analysis

Finite element analysis (FEA) was conducted using the Ansys software package to simulate the magnetic flux density within the air gap. The yoke is composed of SPCC cold-rolled steel, with an isotropic relative permeability of 200. The PM used in the simulation is made of Nd-Fe-B (ND-54 grade), with a coercive force of 9.756×10^5 A/m and a residual induction of 1504 mT at 20 °C. The temperature coefficients of the coercive force and the residual induction are −0.6%/°C and −0.12%/°C, from 20 °C to the maximum limit of 80 °C. The analysis was performed at a temperature of 50 °C; therefore, the temperature-corrected coercive force and residual induction are 8×10^5 A/m and 1450 mT, respectively. Additionally, the mesh convergence analysis, presented in Fig. 14, verifies the stability of the FEA results. The peak magnetic flux density converges as the number of meshing elements approaches 10^5, at which point we selected the FEA model size to achieve a balance between accuracy and computational efficiency.

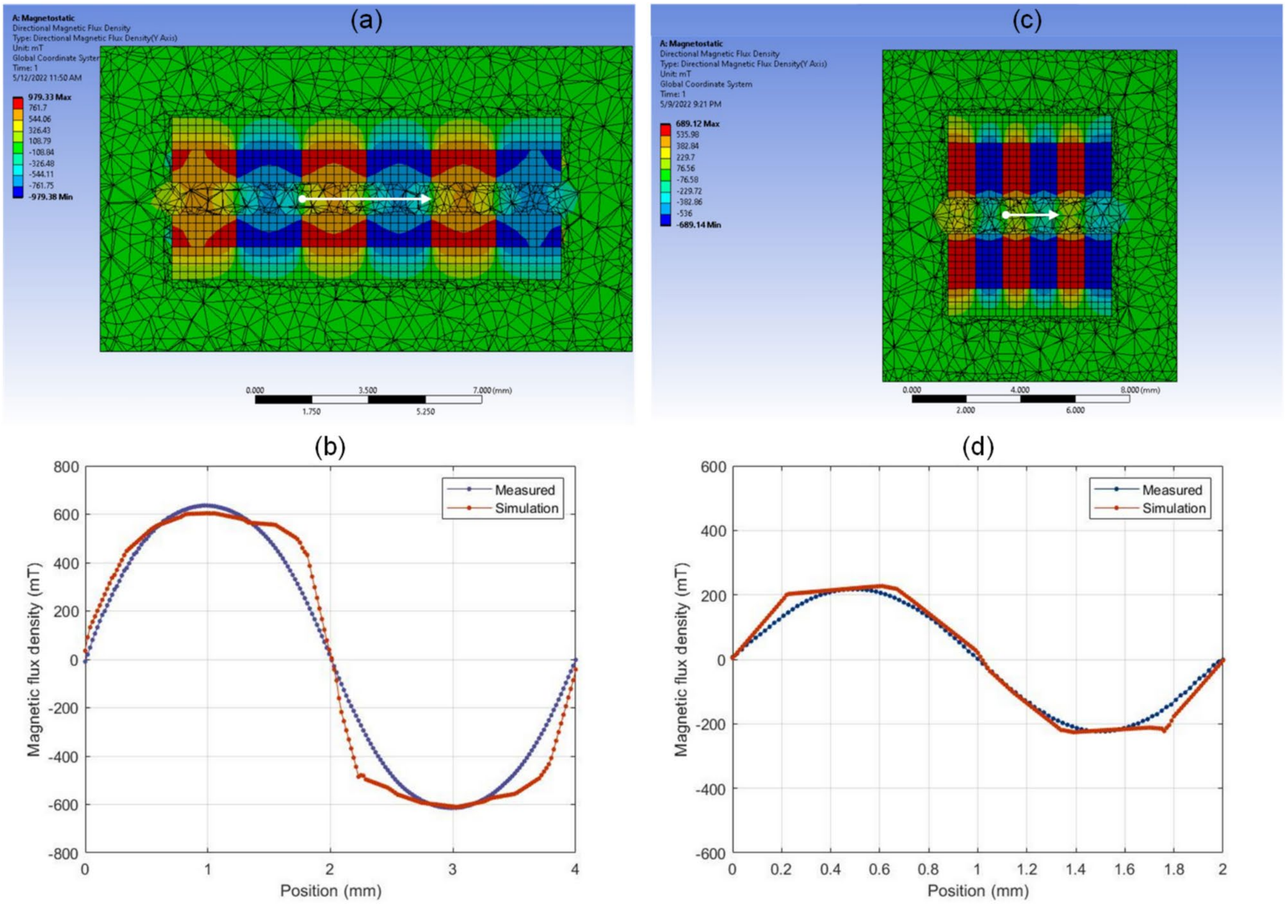

Fig. 15. (**a**) The magnetic field FEA simulation and (**b**) the z-axis magnetic flux density measurement of the 2-phase FLSM air gap. (**c**) and (**d**) are those of 5-phase FLSM air gap.

As shown in Fig. 15, the simulation results reveal a periodic distribution of magnetic flux density. The simulated values of the z-axis magnetic flux density along the white arrow are plotted, alongside real data obtained from a Tesla meter (TM-701, Kanetec). The strong agreement between the simulation and measurement data confirms the validity of our FEA models. It is worth noting that the thickness of the Tesla meter sensor head is 1 mm, which limits the minimum air gap that can be inserted and measured. For future cases where an air gap smaller than 1 mm is required to achieve a stronger magnetic field, our FEA simulation proves valuable in evaluating key parameters.

Thermal analysis

In this study, we use ND-54 grade Nd-Fe-B permanent magnets with a strong residual induction, but their temperature limit of 80 °C poses a restriction. Fig. 16 shows the temperature distribution of an FPCB slider at different phase currents, captured by a thermal camera (TC01A, Fluke). Based on the thermal image, the maximum allowable current should not exceed 0.7 A. For applications involving indirect contact with the human body, we set a more conservative temperature limit of 50 °C, corresponding to a current of 0.4 A. Consequently, the rated phase current is set at 0.4 A in all experiments in this study.

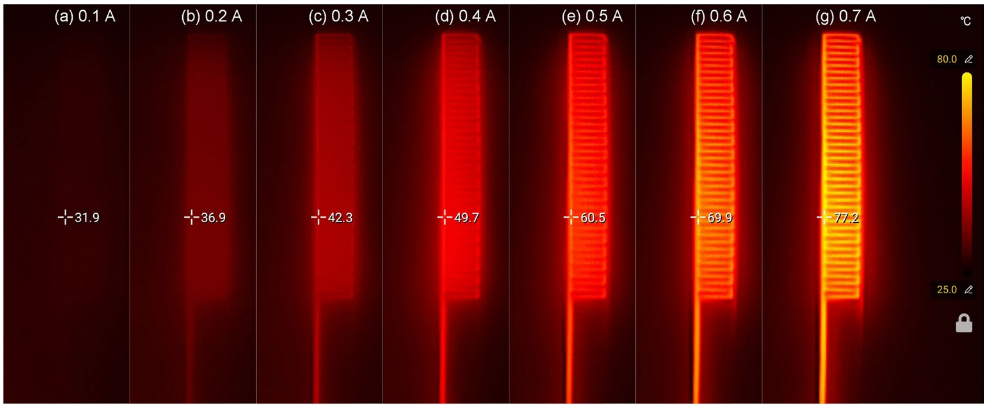

Fig. 16. The temperature distribution of an FPCB slider at different current values from (**a**) 0.1 A to (**g**) 0.7 A.

Data availability

All data generated in this work are included in the published article, supplementary files, or are available from the corresponding author upon request.

Code availability

The computer code generated in this work is available from the corresponding author on request.

Received: 25 September 2024; Accepted: 2 April 2025

References

1. Derammelaere, S. et al. The efficiency of hybrid stepping motors: analyzing the impact of control algorithms. *IEEE Ind. Appl. Mag.* **20**, 50–60. https://doi.org/10.1109/MIAS.2013.2288403 (2014).
2. Lee, Y., Shin, D., Kim, W. & Chung, C. C. Nonlinear H2 control for a nonlinear system with bounded varying parameters: Application to PM stepper motors. *IEEE/ASME Trans. Mechatron.* **22**, 1349–1359. https://doi.org/10.1109/TMECH.2017.2686901 (2017).
3. Kim, W., Shin, D. & Chung, C. C. Microstepping with nonlinear torque modulation for permanent magnet stepper motors. *IEEE Trans. Control Syst. Technol.* **21**, 1971–1979. https://doi.org/10.1109/TCST.2012.2211079 (2013).
4. Bellini, A., Concari, C., Franceschini, G. & Toscani, A. Mixed mode PWM for high performance stepping motors. *IEEE Trans. Ind. Electron.* **54**, 3167–3177. https://doi.org/10.1109/TIE.2007.905929 (2007).
5. Wei, Y., Nguyen, V. H. & Kim, W.-J. A 3-D printed Halbach-cylinder motor with self-position sensing for precision motions. *IEEE/ASME Trans. Mechatron.* **27**, 1489–1497. https://doi.org/10.1109/TMECH.2021.3087523 (2022).
6. Cheng, C.-H. & Hung, S.-K. A piezoelectric two-degree-of-freedom nanostepping motor with parallel design. *IEEE/ASME Trans. Mechatron.* **21**, 2197–2199. https://doi.org/10.1109/TMECH.2015.2502266 (2016).
7. Groenhuis, V., Rolff, G., Bosman, K., Abelmann, L. & Stramigioli, S. Multi-axis electric stepper motor. *IEEE Robot. Autom. Lett.* **6**, 7201–7208. https://doi.org/10.1109/LRA.2021.3097077 (2021).
8. Groenhuis, V., Siepel, F. J. & Stramigioli, S. Magnetic resonance pneumatic stepper motor with multiple concentric shafts output. *IEEE/ASME Trans. Mechatron.* **27**, 2379–2389. https://doi.org/10.1109/TMECH.2021.3102024 (2022).
9. Feng, W. et al. A large-strain and ultrahigh energy density dielectric elastomer for fast moving soft robot. *Nat Commun* **15**, 4222. https://doi.org/10.1038/s41467-024-48243-y (2024).
10. Lee, Y. et al. Liftoff of a soft-actuated micro-aerial-robot powered by triboelectric nanogenerators. *Nano Energy* **126**, 109602. https://doi.org/10.1016/j.nanoen.2024.109602 (2024).
11. Song, Y. et al. A lightweight shape-memory alloy with superior temperature-fluctuation resistance. *Nature* **638**, 965–971. https://doi.org/10.1038/s41586-024-08583-7 (2025).
12. Velvaluri, P. et al. Origami-inspired thin-film shape memory alloy devices. *Sci Rep* **11**, 10988. https://doi.org/10.1038/s41598-021-90217-3 (2021).
13. Ji, X. et al. An autonomous untethered fast soft robotic insect driven by low-voltage dielectric elastomer actuators. *Sci. Robot.* **4**, eaaz6451 (2019).
14. Huang, X., Kumar, K., Jawed, M. K., Ye, Z. & Majidi, C. Soft electrically actuated quadruped (SEAQ)—integrating a flex circuit board and elastomeric limbs for versatile mobility. *IEEE Robot. Autom. Lett.* **4**, 2415–2422. https://doi.org/10.1109/LRA.2019.2903856 (2019).
15. Wang, H. et al. Folding and bending planar coils for highly precise soft angle sensing. *Adv. Mater. Technol.* **5**, 2000659. https://doi.org/10.1002/admt.202000659 (2020).
16. Sandra, K. R., Kumar, A. S. A., George, B. & Kumar, V. J. A linear differential inductive displacement sensor with dual planar coils. *IEEE Sens. J.* **19**, 457–464. https://doi.org/10.1109/JSEN.2018.2877209 (2019).
17. Kawasetsu, T., Niiyama, R. & Kuniyoshi, Y. Flexible and soft inductive tri-axis tactile sensor using liquid metal as sensing target. In *Proceedings of IEEE Sensors*, Montreal, QC, Canada (2019). https://doi.org/10.1109/SENSORS43011.2019.8956736.
18. Chuang, Y.-C., Cheng, T.-Y. & Tsai, Y.-C. Flexible printed circuit board strain sensor embedded in a miniaturized pneumatic finger. *IEEE Sens. J.* **22**, 22456–22463. https://doi.org/10.1109/JSEN.2022.3216278 (2022).
19. Park, Y. et al. Soft, full Wheatstone bridge 3D pressure sensors for cardiovascular monitoring. *npj Flex Electron* **8**, 6. https://doi.org/10.1038/s41528-024-00294-3 (2024).
20. Chen, C.-Y., Chen, C.-L. & Hung, S.-K. Design and implementation of a PCB-based torque sensor with a spiral sensing pattern. *IEEE Trans. Instrum. Meas.* **72**, 7501707. https://doi.org/10.1109/TIM.2023.3241992 (2023).
21. Li, Y. et al. Miura-ori enabled stretchable circuit boards. *npj Flex Electron* **5**, 3. https://doi.org/10.1038/s41528-021-00099-8 (2021).

22. Garrett, A. S. et al. Multichannel mapping of in vivo rat uterine myometrium exhibits both high and low frequency electrical activity in non-pregnancy. *Sci Rep* **14**, 7316. https://doi.org/10.1038/s41598-024-57734-3 (2024).
23. Nagahawatte, N. D. et al. Optimization of pacing parameters to entrain slow wave activity in the pig jejunum. *Sci Rep* **14**, 6038. https://doi.org/10.1038/s41598-024-56256-2 (2024).
24. Tan, V. J. & He, S. Oscillation FPCB micromirror based triangulation laser rangefinder. *J. Micromech. Microeng.* **30**, 095008. https://doi.org/10.1088/1361-6439/ab9b11 (2020).
25. Zuo, H. & He, S. FPCB micromirror-based laser projection availability indicator. *IEEE Trans. Ind. Electron.* **63**, 3009–3018. https://doi.org/10.1109/TIE.2016.2516965 (2016).
26. Zuo, H. & He, S. FPCB ring-square electrode sandwiched micromirror-based laser pattern pointer. *IEEE Trans. Ind. Electron.* **64**, 6319–6329. https://doi.org/10.1109/TIE.2017.2674594 (2017).
27. Periyasamy, K. G. K., Tan, V. J., He, S. & Kourtzanidis, N. External electromagnet FPCB micromirror for large angle laser scanning. *Micromachines* **10**, 667. https://doi.org/10.3390/mi10100667 (2019).
28. Lin, T.-T., Chen, C.-L. & Hung, S.-K. Design and implementation of a laser scanner featuring flexible printed circuit boards. In *Proceedings of IECON*, Brussels, Belgium (2022). https://doi.org/10.1109/IECON49645.2022.9968707.
29. Zuo, H. & He, S. Extra large aperture FPCB mirror based scanning LiDAR. *IEEE/ASME Trans. Mechatron.* **27**, 93–102. https://doi.org/10.1109/TMECH.2021.3058320 (2022).
30. Geng, W. & Zhang, Z. Analysis and implementation of new ironless stator axial-flux permanent magnet machine with concentrated nonoverlapping windings. *IEEE Trans. Energy Convers.* **33**, 1274–1284. https://doi.org/10.1109/TEC.2018.2799172 (2018).
31. Hsu, L.-Y., Yan, G.-J. & Tsai, M.-C. Novel flexible printed circuit windings for slotless linear motor design. In *Proceedings of ICEMS*, Incheon, South Korea, 1578–1582 (2010).
32. Imstepf, D., Baudart, F., Perriard, Y. & Dehez, B. Potential of flex-PCB winding in coreless tubular permanent magnet synchronous machines. In *Proceedings ICEMS*, Chiba, Japan, 1–7 (2016).
33. Kujala, M. et al. Bending reliability of screen-printed vias for a flexible energy module. *npj Flex Electron* **4**, 24. https://doi.org/10.1038/s41528-020-00087-4 (2020).
34. Jang, D. W. et al. Self-heating-induced deterioration of electromechanical performance in polymer-supported metal films for flexible electronics. *Sci Rep* **7**, 12506. https://doi.org/10.1038/s41598-017-12705-9 (2017).
35. Uni-Torque Motor Service Manual No. 127. (Hitachi Ltd., 1977).
36. https://www.vinylengine.com/library/hitachi/uni-torque-motor.shtml (2024)
37. Acarnley, P. *Stepping Motors: A Guide to Theory and Practice*. (4th ed), (Institution of Electrical Engineers, 2002).
38. Oriental Motor's Technical Support Team. 2-phase and 5-phase stepper motor comparison. https://www.orientalmotor.com/stepper-motors/technology/2-phase-vs-5-phase-stepper-motors.html (2024).
39. Morar, A. Driver for 5-phase stepper motor pentagon connection with dedicated ICs. *Procedia Manuf.* **22**, 506–513. https://doi.org/10.1016/j.promfg.2018.03.061 (2018).
40. Devore, J. L. *Probability and Statistics for Engineering and the Sciences* 8th ed, pp. 508–510. (Cengage Learning, 2011).
41. Meng, L. et al. Mathematical modeling of flexible printed circuit configuration: a study in deformation and optimization. *Sci Rep* **14**, 14128. https://doi.org/10.1038/s41598-024-64770-6 (2024).

Acknowledgements

The authors acknowledge the financial support from the National Science and Technology Council, Taiwan, under grant number NSTC 112-2221-E-A49-13 and the technical support from Muherz Inc.

Author contributions

S.-K. Hung conceived the research and designed the prototype; C.-L. Chen, S.-Y. Chu, and Yao-Te Tsai designed the final apparatus, built the system, and performed experiments; S.-K. Hung analyzed data and wrote the manuscript. All authors assisted in editing the manuscript.

Declarations

Competing interests

The authors declare no competing interests.

Additional information

Supplementary Information The online version contains supplementary material available at https://doi.org/10.1038/s41598-025-97104-1.

Correspondence and requests for materials should be addressed to S.-K.H.